Journal of Computational Mathematics
Vol.??, No.?, 200?, 1–22.

http://www.global-sci.org/jcm
doi:??

Improved Harmonic Incompatibility Removal for Susceptibility Mapping via Reduction of Basis Mismatch [*1)]

Chenglong Bao
Yau Mathematical Sciences Center, Tsinghua University, Email: clbao@mail.tsinghua.edu.cn
Jian-Feng Cai
Department of Mathematics, The Hong Kong University of Science and Technology, Email: jfcai@ust.hk
Jae Kyu Choi[2)]
School of Mathematical Sciences, Tongji University, Email: jaycjk@tongji.edu.cn
Bin Dong
Beijing International Center for Mathematical Research and Laboratory for Biomedical Image Analysis Beijing Institute of Big Data Research, Peking University, Email: dongbin@math.pku.edu.cn
Ke Wei
School of Data Science, Fudan University, Email: kewei@fudan.edu.cn

Abstract

In quantitative susceptibility mapping (QSM), the background field removal is an essential data acquisition step because it has a significant effect on the restoration quality by generating a harmonic incompatibility in the measured local field data. Even though the sparsity based first generation harmonic incompatibility removal (1GHIRE) model has achieved the performance gain over the traditional approaches, the 1GHIRE model has to be further improved as there is a basis mismatch underlying in numerically solving Poisson's equation for the background removal. In this paper, we propose the second generation harmonic incompatibility removal (2GHIRE) model to reduce a basis mismatch, inspired by the balanced approach in the tight frame based image restoration. Experimental results shows the superiority of the proposed 2GHIRE model both in the restoration qualities and the computational efficiency.

Mathematics subject classification: 35R30, 42B20, 45E10, 65K10, 68U10, 90C90, 92C55
Key words: Quantitative susceptibility mapping, magnetic resonance imaging, deconvolution, partial differential equation, harmonic incompatibility removal, (tight) wavelet frames, sparse approximation

1. Introduction

Quantitative susceptibility mapping (QSM) [1] is a novel noninvasive imaging method which visualizes the magnetic susceptibility distribution of a human body from a given local field perturbation data measured from the magnetic resonance imaging (MRI) signal. The magnetic susceptibility χ is a physical property of a material which relates a magnetization $\mathbf{M} = (M_1, M_2, M_3)$ and a magnetic field $\mathbf{H} = (H_1, H_2, H_3)$ through $\mathbf{M} = \chi\mathbf{H}$ [2]. The physiological and/or pathological processes alter the scalar tissue magnetic susceptibilities [2], whose visualization is becoming reasonably robust and accurate for

[*] Received ???? ??, 200? / Revised version received ???? ??, 200? / Accepted ???? ??, 200? /
[1)] The research of the first author is supported in part by the NSFC Youth Program 11901338. The research of the second author is supported by the Hong Kong Research Grant Council (HKRGC) GRF 16306317 and 16309219. The research of the third author is supported by the NSFC Youth Program 11901436 and the Fundamental Research Program of Science and Technology Commission of Shanghai Municipality (20JC1413500. The research of the fourth author is supported by the NSFC grant 11831002. The research of the fifth author is supported by the National Natural Science Foundation of China Youth Program grant 11801088 and the Shanghai Sailing Program 18YF1401600.
[2)] Corresponding author: jaycjk@tongji.edu.cn

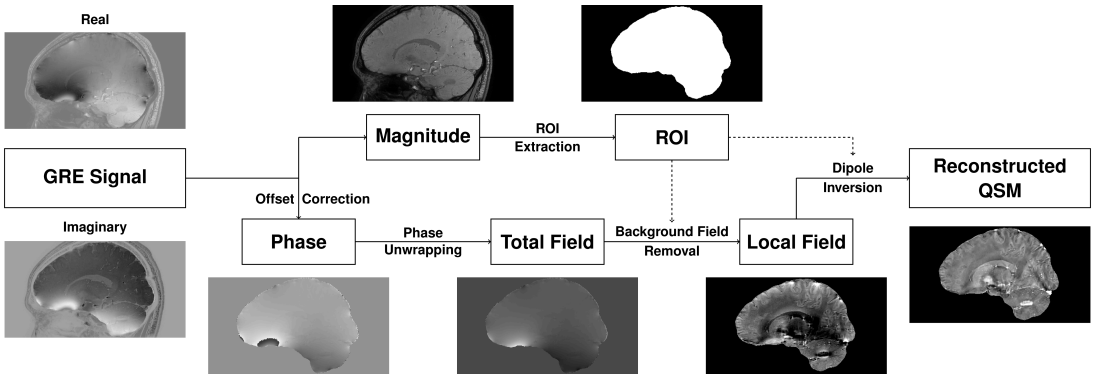

Fig. 1.1. Schematic diagram of QSM reconstruction process. Dashed line indicates that the extracted ROI is used for the background removal and/or the dipole inversion.

practical applications [3]. Consequently, QSM recently covers a various range of clinical applications such as demyelination, inflammation, and iron overload in multiple sclerosis [4], neurodegeneration and iron overload in Alzheimer's disease [5], Huntington's disease [6], changes in metabolic oxygen consumption [7], hemorrhage including microhemorrhage and blood degradation [8], bone mineralization [9], and drug delivery using magnetic nanocarriers [10].

QSM is based on the post processing the phase data of a complex gradient echo (GRE) signal because the magnetic susceptibility distribution in an MR scanner induces the *total field* which can be captured by the phase shifts in the GRE signal [11, 12]. The post processing consists of the four stages; the phase offset correction, the phase unwrapping, the background field removal, and the dipole inversion; see Figure 1.1 for the brief overview of the process. Throughout this paper, we only focus on the background field removal to estimate the *local field* induced by the susceptibility in the region of interest (ROI) $\Omega \subseteq \mathbb{R}^3$ which occupies the water and brain tissues, and the dipole inversion to reconstruct and visualize the susceptibility distribution in the ROI Ω using the measured local field data. Interested readers may refer to e.g. [12] and references therein for more details on the other QSM stages such as the phase offset correction, the phase unwrapping, etc.

Given the local field f, the susceptibility reconstruction is based on solving the following convolution relation [13–15]:

$$f(\boldsymbol{x}) = \mathrm{pv} \int_\Omega d(\boldsymbol{x} - \boldsymbol{y})\chi(\boldsymbol{y})\mathrm{d}\boldsymbol{y}, \tag{1.1}$$

where pv denotes the principal value [16] of the singular integral with the kernel d:

$$d(\boldsymbol{x}) = \frac{2x_3^2 - x_1^2 - x_2^2}{4\pi|\boldsymbol{x}|^5}.$$

In the frequency domain, (1.1) reads

$$\mathcal{F}(f)(\boldsymbol{\xi}) = \mathcal{D}(\boldsymbol{\xi})\mathcal{F}(\chi)(\boldsymbol{\xi}) = \left(\frac{1}{3} - \frac{\xi_3^2}{|\boldsymbol{\xi}|^2}\right)\mathcal{F}(\chi)(\boldsymbol{\xi}) \tag{1.2}$$

where $\mathcal{D} = \mathcal{F}(d)$ is the Fourier transform of d, and by the definition of pv, $\mathcal{D}(\mathbf{0}) = 0$ [1, 17]. From (1.2), we can easily see that the inverse problem is ill-posed as $\mathcal{D}(\boldsymbol{\xi}) = 0$ for $\boldsymbol{\xi}$ satisfying $\xi_1^2 + \xi_2^2 - 2\xi_3^2 = 0$; whenever the measured local field data f contains the incompatibilities, the reconstructed susceptibility image contains artifacts [18].

1.1. Effects of background field removal on susceptibility restoration

In the literature, there have been extensive studies related to the noise (e.g. [19,20]), while the incompatibilities arising from the background removal have received little attention. In fact, the background field removal is one of the most crucial data acquisition steps as the incompatibilities generated from this step is different from the additive noise, which has a significant effect on the recovery unless it is appropriately suppressed [21].

For the brief explanation on the background field removal, assume that the susceptibility χ is compactly supported (not necessarily strictly supported in Ω) on $\mathbb{R}^3$. Then the induced total field b satisfies the following partial differential equation (PDE):

$$-\Delta b = P(D)\chi := \left(-\frac{1}{3}\Delta + \frac{\partial^2}{\partial x_3^2}\right)\chi. \tag{1.3}$$

Interested readers may consult [21] and the references therein for the detailed derivation. Hence, b can be expressed as the following Newtonian potential (e.g. [22]):

$$b(\boldsymbol{x}) = \int_{\mathbb{R}^3} \Phi(\boldsymbol{x}-\boldsymbol{y})\left(-\frac{1}{3}\Delta_y + \frac{\partial^2}{\partial y_3^2}\right)\chi(\boldsymbol{y})\mathrm{d}\boldsymbol{y} \tag{1.4}$$

where $\Phi(\boldsymbol{x}) = 1/(4\pi|\boldsymbol{x}|)$ is the fundamental solution of $-\Delta$.

Comparing (1.1) and (1.4), and together with [18, Proposition A.1], we can see that the goal of background field removal is to *reduce the domain of integration from* $\mathbb{R}^3$ *to* Ω. Namely, given a (limited) total field b, we may obtain the local field data f by solving

$$-\Delta f = 1_\Omega\,(-\Delta b) \tag{1.5}$$

where 1_Ω is the characteristic function of Ω. However, since (1.5) is underdetermined, we need additional information for the unique estimation [23]. One benchmark approach is imposing the following Dirichlet boundary condition

$$\begin{cases} -\Delta f = -\Delta b & \text{in } \Omega \\ f = 0 & \text{on } \partial\Omega. \end{cases} \tag{1.6}$$

Even though (1.6) admits the unique solution, its solution is represented as the Green's function $G(\boldsymbol{x},\boldsymbol{y})$ associated to Ω [24]. Recently, based on this fact, the authors in [21] show that the solution to (1.6) is represented as

$$f(\boldsymbol{x}) = \int_\Omega \Phi(\boldsymbol{x}-\boldsymbol{y})\left(-\frac{1}{3}\Delta_y + \frac{\partial^2}{\partial y_3^2}\right)\chi(\boldsymbol{y})\mathrm{d}\boldsymbol{y} + v(\boldsymbol{x}) \tag{1.7}$$

where v satisfies

$$\int_{\mathbb{R}^3} v(\boldsymbol{x})\,(-\Delta\varphi)\,(\boldsymbol{x})\mathrm{d}\boldsymbol{x} = \int_{\partial\Omega}\left[\frac{\partial v_\mathrm{i}}{\partial \boldsymbol{n}}(\boldsymbol{x}) - \frac{\partial v_\mathrm{e}}{\partial \boldsymbol{n}}(\boldsymbol{x})\right]\varphi(\boldsymbol{x})\mathrm{d}\sigma(\boldsymbol{x}) \tag{1.8}$$

for $\varphi \in C_0^\infty(\mathbb{R}^3)$, and

$$\frac{\partial v_\mathrm{i}}{\partial \boldsymbol{n}} - \frac{\partial v_\mathrm{e}}{\partial \boldsymbol{n}} \neq 0 \quad \text{almost everywhere on } \partial\Omega \tag{1.9}$$

whenever $P(D)\chi \neq 0$ in Ω. Here, v_{i} and v_{e} are the restriction of v in $\overline{\Omega}$ and $\mathbb{R}^3 \setminus \Omega$ respectively, $\boldsymbol{n}$ is the outward unit normal vector of $\partial\Omega$, and $\boldsymbol{\sigma}$ is the surface measure on $\partial\Omega$. Note that v_{i} and v_{e} are the solutions of

$$-\Delta v_{\mathrm{i}} = 0 \quad \text{in} \quad \Omega \tag{1.10}$$

$$-\Delta v_{\mathrm{e}} = 0 \quad \text{in} \quad \mathbb{R}^3 \setminus \overline{\Omega} \tag{1.11}$$

$$v_{\mathrm{i}} = v_{\mathrm{e}} = -b \quad \text{on} \quad \partial\Omega, \tag{1.12}$$

respectively, which shows that v is continuous on $\partial\Omega$ due to the common boundary condition (1.12).

This means that even in the noise-free case, the local field f obtained from (1.6) contains an incompatibility harmonic except on $\partial\Omega$, which we shall call v the *harmonic incompatibility* in what follows. Since v is smooth, analytic, and satisfies the mean value property except on $\partial\Omega$ [24], it has slow variations compared to the additive noise [21]. Hence, it mostly affects the low frequency components in f while the noise mainly affects the high frequency components. Together with the ill-posedness of (1.1), the incompatibility in low frequency components of f leads to the shadow artifacts in the reconstructed image, while that in high frequency components leads to the streaking artifacts [21]. However, since the traditional single system based regularization approaches cannot suppress both incompatibilities simultaneously, the unsuppressed incompatibility in turn leads to the erroneous susceptibility restoration results.

1.2. Motivations and contributions of our approach

Recently, the authors in [21] further observed that $-\Delta v$ is sparse in the discrete setting, and proposed the following first generation harmonic incompatibility removal (1GHIRE) model for the susceptibility reconstruction

$$\min_{\chi,v} \ \frac{1}{2}\|A\chi + v - f\|_{\Xi}^2 + \lambda\|\mathcal{L}v\|_1 + \|\gamma \cdot W\chi\|_{1,2} \tag{1.13}$$

where A denotes the discretization of the forward operator in (1.7), $\mathcal{L}$ is the discrete Laplacian, W is a given wavelet frame transformation with L level of decomposition, and $\gamma = \{\gamma_l : l = 0, \cdots, L-1\}$ is a regularization parameter imposing different penalization on each level. (The detailed introductions of the notation will be postponed until subsection 2.1). By imposing the sparse regularization of $\mathcal{L}v$, 1GHIRE model (1.13) adopts the idea of two system regularization [25, 26] so that the incompatibility other than the additive noise can be taken into account.

Even though the above 1GHIRE model has achieved the susceptibility image reconstruction with less artifacts compared to the traditional single system based regularization approaches, it has to be further improved. It should be noted that the ℓ_1 norm which promotes the sparsity of $\mathcal{L}v$ in the entire image domain may not be capable of fully reflecting the harmonic incompatibility v except on $\partial\Omega$, albeit it can be a way of relaxation when considering the error source of the forward model in QSM. Since the measured data f can contain the outliers in Ω whose intensity is stronger than $\mathcal{L}v$ [11], $\|\mathcal{L}v\|_1$ in (1.13) may capture such outliers, leading to the erroneous removal in the harmonic incompatibility. Most importantly, since the discrete images and the ROI defined on the regular grids are available only, there exists a *basis mismatch* arising from numerically solving (1.6); that is, a mismatch between the true supports of $-\Delta v$ in the continuous domain and those of $\mathcal{L}v$ in the discrete setting. Such a basis mismatch can degrade the sparsity of $\mathcal{L}v$, which may in turn lead to the degradation of restoration quality. Indeed, even though we can consider the following variant model

$$\min_{\chi,v} \ \frac{1}{2}\|A\chi + v - f\|_{\Xi}^2 + \lambda\|(\mathcal{L}v)_{\Lambda^c}\|_p^p + \|\gamma \cdot W\chi\|_{1,2} \tag{1.14}$$

where $p = 1$ or 2, and Λ is the estimated support of $\mathcal{L}v$, the underlying basis mismatch results in the restoration result highly sensitive to the estimation of Λ.

In this paper, we improve the previous 1GHIRE model (1.13) to reduce the basis mismatch underlying in solving (1.6). The proposed second generation harmonic incompatibility removal (2GHIRE) model is inspired by the balanced approach (e.g. [27–29]) in the tight frame based image restoration. More specifically, since the basis mismatch hampers $\mathcal{L}v$ from being sparse on the discrete grid, we provide a flexibility in sparse approximation of $\mathcal{L}v$ instead of directly enforcing the properties of $-\Delta v$ mentioned in subsection 1.1. Finally, experiments on both brain phantom and in-vivo MR data consistently show that the proposed 2GHIRE model is robust to the estimation of Λ, achieving further improvements over the previous 1GHIRE model and its variants.

1.3. Organization of paper

In section 2, we introduce the proposed 2GHIRE model to reduce a basis mismatch, followed by an alternating minimization algorithm. In section 3, we present experimental results for both brain phantom and in vivo MR data, and section 4 concludes this paper with some future directions.

2. Second generation harmonic incompatibility removal (2GHIRE) model

2.1. Proposed 2GHIRE susceptibility reconstruction model

We begin with introducing some notations. Let $\mathbb{O} = \{0, \cdots, N_1 - 1\} \times \{0, \cdots, N_2 - 1\} \times \{0, \cdots, N_3 - 1\}$ denote the set of indices of $N_1 \times N_2 \times N_3$ grids, and let $\Omega \subseteq \mathbb{O}$ denote the set of indices corresponding to the ROI. Denote $\partial\Omega$ to be the set of indices where the boundary condition in (1.6) is active. Finally, the space of real valued functions defined on $\mathbb{O}$ is denoted as $\mathcal{I}_3 \simeq \mathbb{R}^{N_1 \times N_2 \times N_3}$.

As in [21], we model the (noisy) measured local field data $f \in \mathcal{I}_3$ obtained from (1.6) (and satisfying $f = 0$ in $\mathbb{O} \setminus \Omega$) as

$$f = A\chi + v + \eta. \tag{2.1}$$

Here, $A = \mathcal{F}^{-1}\mathcal{D}\mathcal{F}$ denotes the discretization of the forward operator in (1.7), $\chi \in \mathcal{I}_3$ denotes the unknown true susceptibility image supported in Ω, $v \in \mathcal{I}_3$ is the incompatibility arising from solving (1.6), and η is the additive noise.

In the ideal discrete setting where the boundary in the continuous domain is well aligned with the discrete grid $\mathbb{O}$, the properties of the harmonic incompatibility v read as follows: there exists $w \in \mathcal{I}_3$ such that

$$\mathcal{L}v = w \quad \text{and} \quad \text{supp}(w) = \partial\Omega \tag{2.2}$$

with the discrete Laplacian $\mathcal{L}$, so that we have

$$\|\mathcal{L}v\|_0 = |\partial\Omega| \ll |\mathbb{O}|. \tag{2.3}$$

However, it is in general difficult to directly apply (2.2) into the susceptibility reconstruction model because 1) the real MRI data may not exactly satisfy (2.2) due to the (possibly) anisotropic spatial resolution [21]; 2) since the discrete magnitude and phase images are available only, it is inevitable to have a basis mismatch [30, 31] between the true support of $-\Delta v$ in the continuous domain and the

discrete grid, which in turn leads to to the loss of (2.2) in the discrete setting. As a consequence, we propose the second generation harmonic incompatibility removal (2GHIRE) model as follows:

$$\begin{aligned} &\min_{\chi,v,w} \frac{1}{2}\|A\chi + v - f\|_\Xi^2 + \frac{\lambda}{2}\|\mathcal{L}v - w\|_2^2 + \|\gamma \cdot W\chi\|_{1,2} \\ &\text{subject to } \ \mathcal{P}_{\Lambda^c} w = 0 \ \text{ and } \ \|w\|_0 \le r \end{aligned} \tag{2.4}$$

where Λ denotes the estimation of $\mathrm{supp}(\mathcal{L}v)$, r is an estimated model order, $\mathcal{P}_{\mathcal{A}}$ is the projection operator onto a set $\mathcal{A}$, and the ℓ_0 norm constraint comes from the fact that the circulant lifting is diagonalized by the unitary discrete Fourier transform (i.e. $\mathrm{rank}\,(\mathcal{C}\widehat{w}) = \|w\|_0$). Here, $\|\cdot\|_\Xi^2 = \langle \Xi\cdot, \cdot\rangle$ where the SNR weight Ξ is estimated from the MRI [14, 32], and $\|\gamma \cdot W\chi\|_{1,2}$ is the isotropic ℓ_1 norm of the B-spline wavelet frame coefficients defined as

$$\|\gamma \cdot W\chi\|_{1,2} := \sum_{\boldsymbol{k}\in\mathbb{O}} \sum_{l=0}^{L-1} \gamma_l[\boldsymbol{k}] \left(\sum_{\boldsymbol{\alpha}\in\mathbb{B}} \left| (W_{l,\boldsymbol{\alpha}}\chi)\,[\boldsymbol{k}] \right|^2 \right)^{1/2} \tag{2.5}$$

where $\mathbb{B} = \{0, 1, \cdots, m\}^3 \setminus \{\mathbf{0}\}$ denotes the framelet band [33]. Interested readers can refer to e.g. [33,34] and the references therein for the introduction on the B-spline wavelet frames.

Note that numerous variational regularizations for the susceptibility reconstruction were already proposed in the literature. The most widely used variational approaches include total variation [35], total generalized variation [36], weighted total variation for morphological consistency [37], and so on. However, since $\mathcal{D}(\mathbf{0}) = 0$, the χ subproblem in the alternating direction method of multipliers (ADMM) for the variational susceptibility reconstruction models has a rank deficient system matrix. Hence, we may need additional prior information such as the zero susceptibility value in the cerebrospinal fluid region [38] for the stable reconstruction. In contrast, by using the tight frame regularization, the system matrix of χ subproblem has a full column rank, which leads to the computational efficiency over the existing variational methods [21].

In the 2GHIRE model (2.4), the first constraint ($\mathcal{P}_{\Lambda^c} w = 0$) reflects (2.2) so that we can prevent w from capturing the outliers in Ω [11]. In addition, it is easy to see that the sparsity constraint ($\|w\|_0 \le r$) reflects (2.3). Finally, similar to the balanced approach (e.g. [27–29]) in the tight frame based image restoration, the term $\|\mathcal{L}v - w\|_2^2$ balances the distance between $\mathcal{L}v$ and w where w satisfies the aforementioned constraints. Obviously, if we set $\lambda = \infty$, then $w = \mathcal{L}v$, and (2.4) becomes

$$\begin{aligned} &\min_{\chi,v} \frac{1}{2}\|A\chi + v - f\|_\Xi^2 + \|\gamma \cdot W\chi\|_{1,2} \\ &\text{subject to } \ \mathcal{P}_{\Lambda^c}(\mathcal{L}v) = 0 \ \text{ and } \ \|\mathcal{L}v\|_0 \le r. \end{aligned} \tag{2.6}$$

For our purpose, the choice of (2.4) instead of (2.6) and the reasons are as follows: first of all, $\mathcal{L}v$ may not exactly satisfy (2.2) due to the basis mismatch arising in solving (1.6) numerically with a given discrete total field data and a given discrete ROI. Since this basis mismatch degrades the sparsity of $\mathcal{L}v$ on $\mathbb{O}$, the restoration result will be highly sensitive to the choice of Λ when we directly impose (2.2) and (2.3). In addition, the local field f is in general dominated by the errors near the boundary because the GRE signal lacks information outside the ROI [12]. This means that, the direct constraint will in fact restore a harmonic incompatibility v induced by the errors near the boundary rather than by information of (unknown) $-A\chi$ on $\partial\Omega$ described in [21, Theorem 2.2]. This erroneous restoration of v affects the low frequency components of f again, leading to the new shadow artifacts in the restored images. In contrast, the proposed 2GHIRE model (2.4) does not strictly require that $\mathcal{L}v$ satisfy the above properties (2.2) and (2.3). By balancing the distance between $\mathcal{L}v$ which does not satisfy the constraint

in general and w which satisfies the constraints instead, we expect to achieve the better suppression of incompatibilities as well as the restoration results more robust to the estimation of Λ than (2.6).

Finally, we mention that the proposed 2GHIRE model is not limited to (2.4). In fact, as mentioned in [21], the nonlinear fidelity term $\frac{1}{2}\left\|m\left(e^{i(A\chi+v)\omega_0 B_0 TE} - e^{ib_l\omega_0 B_0 TE}\right)\right\|_2^2$ can be used to further compensate the errors arising in the phase unwrapping, which will be more appropriate to the GRE signal model [3, 19]. Indeed, it is also worth noting that (1.14) with $p = 2$ can be viewed as the linearized version of the nonlinear model in [11]. Nonetheless, we forgo further discussions on the nonlinear variants as it is beyond the scope of this paper.

2.2. Numerical algorithm

Overall alternating minimization algorithm is as follows: for $n = 0, 1, \cdots$,

$$(\chi_{n+1}, v_{n+1}) = \underset{\chi,v}{\operatorname{argmin}} \ \frac{1}{2}\|A\chi + v - f\|_\Xi^2 + \frac{\lambda}{2}\|\mathcal{L}v - w_n\|_2^2 + \|\gamma \cdot W\chi\|_{1,2} \tag{2.7}$$

$$w_{n+1} = \underset{\substack{\mathcal{P}_{\Lambda^c} w = 0 \\ \|w\|_0 \le r}}{\operatorname{argmin}} \ \|w - \mathcal{L}v_{n+1}\|_2^2 \tag{2.8}$$

i.e. we update (χ, v) and w alternatively.

To solve (2.7), we use the split Bregman algorithm given in [32] in the framework of alternating direction method of multipliers (ADMM) [39]. For the completeness, we present the full details of the split Bregman algorithm for solving (2.7): for $m = 0, 1, \cdots$,

$$\begin{bmatrix}\chi_{m+1} \\ v_{m+1}\end{bmatrix} = \operatorname{argmin} \ \frac{\beta}{2}\|A\chi + v - e_m + \widetilde{e}_m\|_2^2 + \frac{\beta}{2}\|W\chi - c_m + \widetilde{c}_m\|_2^2 + \frac{\lambda}{2}\|\mathcal{L}v - w_n\|_2^2 \tag{2.9}$$

$$c_{m+1} = \operatorname{argmin} \ \|\gamma \cdot c\|_{1,2} + \frac{\beta}{2}\|c - W\chi_{m+1} - \widetilde{c}_m\|_2^2 \tag{2.10}$$

$$e_{m+1} = \operatorname{argmin} \ \frac{1}{2}\|e - f\|_\Xi^2 + \frac{\beta}{2}\|e - A\chi_{m+1} - v_{m+1} - \widetilde{e}_m\|_2^2 \tag{2.11}$$

$$\widetilde{c}_{m+1} = \widetilde{c}_m + W\chi_{m+1} - c_{m+1} \tag{2.12}$$

$$\widetilde{e}_{m+1} = \widetilde{e}_m + A\chi_{m+1} + v_{m+1} - e_{m+1} \tag{2.13}$$

where we omit the outer iteration subscript n for the notational simplicity.

Note that each subproblem has a closed form solution and it can be written as

$$\begin{bmatrix}\chi_{m+1} \\ v_{m+1}\end{bmatrix} = \begin{bmatrix}A^TA + I & A^T \\ A & I + \lambda/\beta\mathcal{L}^T\mathcal{L}\end{bmatrix}^{-1}\begin{bmatrix}A^T(e_m - \widetilde{e}_m) + W^T(c_m - \widetilde{c}_m) \\ e_m - \widetilde{e}_m + \lambda/\beta\mathcal{L}^T w_n\end{bmatrix} \tag{2.14}$$

$$c_{m+1} = \mathcal{T}_{\gamma/\beta}\left(W\chi_{m+1} + \widetilde{c}_m\right) \tag{2.15}$$

$$e_{m+1} = (\Xi + \beta I)^{-1}\left\{\Xi f + \beta\left(A\chi_{m+1} + v_{m+1} + \widetilde{e}_m\right)\right\} \tag{2.16}$$

$$\widetilde{c}_{m+1} = \widetilde{c}_m + W\chi_{m+1} - c_{m+1} \tag{2.17}$$

$$\widetilde{e}_{m+1} = \widetilde{e}_m + A\chi_{m+1} + v_{m+1} - e_{m+1}. \tag{2.18}$$

It is not hard to see that the system matrix in (2.14) is invertible, and the four submatrices can be diagonalized by the fast Fourier transform. Hence, we can easily solve (2.14) by using the pointwise Gaussian elimination or the pointwise Kramer's rule in the frequency domain. For (2.15), $\mathcal{T}_\gamma$ is the isotropic soft thresholding in [33]: given c defined as

$$c = \{c_{l,\boldsymbol{\alpha}} : (l, \boldsymbol{\alpha}) \in (\{0, \cdots, L-1\} \times \mathbb{B}) \cup \{(L-1, \mathbf{0})\}\}$$

Algorithm 2.1 Numerical algorithm for the 2GHIRE model (2.4)

Initialization: χ_0, v_0, w_0, c_0, e_0, $\widetilde{c}_0$, $\widetilde{e}_0$

for $n = 0, 1, 2, \cdots$ **do**

Update

$$\begin{bmatrix}\chi_{n+1}\\ v_{n+1}\end{bmatrix} = \begin{bmatrix}A^TA + I & A^T\\ A & I + \lambda/\beta\mathcal{L}^T\mathcal{L}\end{bmatrix}^{-1}\begin{bmatrix}A^T(e_n - \widetilde{e}_n) + W^T(c_n - \widetilde{c}_n)\\ e_n - \widetilde{e}_n + \lambda/\beta\mathcal{L}^T w_n\end{bmatrix}$$

$$\begin{aligned}
c_{n+1} &= \mathcal{T}_{\gamma/\beta}\left(W\chi_{n+1} + \widetilde{c}_n\right)\\
e_{n+1} &= (\Xi + \beta I)^{-1}\left\{\Xi f + \beta\left(A\chi_{n+1} + v_{n+1} + \widetilde{e}_n\right)\right\}\\
\widetilde{c}_{n+1} &= \widetilde{c}_n + W\chi_{m+1} - c_{n+1}\\
\widetilde{e}_{n+1} &= \widetilde{e}_n + A\chi_{n+1} + v_{n+1} - e_{n+1}\\
\widetilde{w}_{n+1} &= \mathcal{P}_\Lambda\left(\mathcal{L}v_{n+1}\right)\\
w_{n+1} &= \mathcal{P}_{\Lambda_{n+1}}\widetilde{w}_{n+1},
\end{aligned}$$

where Λ_{n+1} is the set of indices corresponding to r largest absolute values in $\widetilde{w}_{n+1}$.

end for

and $\gamma = \{\gamma_l : l = 0, 1, \cdots, L-1\}$ with $\gamma_l \geq 0$, $\mathcal{T}_\gamma(c)$ is defined as

$$\left(\mathcal{T}_\gamma(c)\right)_{l,\boldsymbol{\alpha}}[\boldsymbol{k}] = \begin{cases} c_{l,\boldsymbol{\alpha}}[\boldsymbol{k}], & (l,\boldsymbol{\alpha}) = (L-1, \mathbf{0})\\ \max\left(R_l[\boldsymbol{k}] - \gamma_l[\boldsymbol{k}], 0\right)\dfrac{c_{l,\boldsymbol{\alpha}}[\boldsymbol{k}]}{R_l[\boldsymbol{k}]}, & (l,\boldsymbol{\alpha}) \in \{0,\cdots,L-1\}\times\mathbb{B}\end{cases}$$

where $R_l[\boldsymbol{k}] = \left(\sum_{\boldsymbol{\alpha}\in\mathbb{B}}\left|c_{l,\boldsymbol{\alpha}}[\boldsymbol{k}]\right|^2\right)^{1/2}$ for $\boldsymbol{k} \in \mathbb{O}$. For (2.16), $\Xi + \beta I$ is simply a diagonal matrix and thus, no matrix inversion is needed.

For (2.8), we apply the following alternating projection:

$$\widetilde{w}_{n+1} = \mathcal{P}_\Lambda\left(\mathcal{L}v_{n+1}\right) \tag{2.19}$$

$$w_{n+1} = \mathcal{P}_{\Lambda_{n+1}}\widetilde{w}_{n+1} \tag{2.20}$$

where Λ_{n+1} is the set of indices corresponding to r largest absolute values in $\widetilde{w}_{n+1}$.

Finally, we mention that, to get an exact solution, we need to choose $(\chi_{n+1}, v_{n+1}) = (\chi_{n,\infty}, v_{n,\infty})$. However, it would be too conservative to use infinite steps of inner iterations. The reason is that both (χ_n, v_n) and w_n at each iteration step might not be accurate enough, and accuracy obtained by the infinite loop will be wasted, which is typical in the split Bregman algorithm [40, 41]. Hence, we only need to perform one iteration in (2.7) for computational efficiency, and we summarize the complete iteration that will be used in our algorithm for solving the 2GHIRE model (2.4) in Algorithm 2.1. Unfortunately, since the 2GHIRE model is nonconvex, the convergence of Algorithm 2.1 in theory keeps an open issue [42, 43]. Nevertheless, we empirically observe that Algorithm 2.1 is fast convergent with the smaller number of iterations than other models.

3. Experiments

In this section, we present some experimental results on brain phantom in [44] and the single echo (SE) data used in the QSM 2016 reconstruction challenge [45], and the multi echo (ME) data in [18] to compare the proposed 2GHIRE model (2.4) with other existing reconstruction methods. The brain

phantom images are available on Cornell MRI Research Lab webpage[1)] , and the SE data are available on Neuroimaging Research Unit-Medical University of Graz webpage[2)] . In the literature, the regularization based approaches outperform the direct approaches including the truncated K-space division [46] and the Tikhonov regularization [47]. In addition, since it is demonstrated in [21] that taking the harmonic incompatibility v in the measured local field f into account leads to the performance gain over the traditional single system based approaches such as the integral approach and the differential approaches, we focus on the comparison of the 2GHIRE model (2.4) with the 1GHIRE model (1.13), its variants (1.14) with both $p = 1$ and 2, and the model (2.6). All experiments are implemented on MATLAB R2014a running on a laptop with 64GB RAM and Intel(R) Core(TM) CPU i7-8750H at 2.20GHz with 6 cores.

In all models, we choose W to be the tensor product Haar framelet transform with 1 level of decomposition to avoid the memory storage problem (Note, however, that the decomposition level and the choice of W will do affect the restoration results), and we use the standard centered difference for $\mathcal{L}$. Most importantly, to compare the effects of Λ on the restoration results, we estimate Λ from Ω using 1) the finite difference $\mathcal{L}$; and 2) the spherical mean value (SMV) filter [48] with radius 1.5mm, which will be referred as "thin Λ" and "thick Λ" respectively. For the parameters, we choose γ in (2.5) of the form $\gamma = \{\nu 2^{-l} : l = 0, \cdots, L-1\}$ with $\nu > 0$, and the detailed choices are summarized in Table (3.1) for each case and each model. Empirically, we observe that the reconstructed images contain more artifacts as ν becomes smaller while the larger ν leads to the overly smoothed restoration results. In addition, when λ is large, the estimated harmonic incompatibility v becomes smooth near the boundary of ROI. It is also worth noting that the proposed 2GHIRE model is relatively insensitive to the choice of r. As a rule of a thumb, it suffices to choose r to be $0.02 \sim 0.025\%$ of $|\mathbb{O}|$. Based on this observation, the parameters are chosen manually to balance indices and visual qualities. For the stopping criterion of Algorithm 2.1, we use

$$\frac{\|\chi_{n+1} - \chi_n\|_2}{\|\chi_{n+1}\|_2} \leq \varepsilon = 5 \times 10^{-3}. \tag{3.1}$$

The models (1.13), (1.14), and (2.6) are solved using the split Bregman algorithm similar to our algorithm with the same stopping criterion (3.1). In all cases, we set the maximum allowable number of iterations to be 600, and all models are initialized with $\chi_0 = v_0 = w_0 = 0$. Finally, for the quantitative comparison of each reconstruction model, we use the root mean square error (RMSE), the structural similarity index map (SSIM) [49].

3.1. Brain phantom experiments

The brain phantom experiments is implemented by simulating the 12 equispaced multi echo GREs at 3T with TE ranging from 2.5msec to 30msec, using the $256 \times 256 \times 98$ image with spatial resolution $0.9375 \times 0.9375 \times 1.5\text{mm}^3$. More precisely, we synthesize the local field data f in Figure 3.1(f) as follows. We first generate the true magnitude image $\widetilde{m}$, and simulate the true total field $\widetilde{b}$ by adding four background susceptibility sources in the true susceptibility image to generate the background field. Using $\widetilde{m}$ and $\widetilde{b}$, we generate the noisy multi echo complex GRE signal by

$$I[\boldsymbol{k}, t] = \widetilde{m}[\boldsymbol{k}] \exp\{-i\widetilde{b}[\boldsymbol{k}]\omega_0 B_0 TE[t]\} + \eta[\boldsymbol{k}, t], \qquad \boldsymbol{k} \in \mathbb{O}, \ \& \ t = 1, \cdots, 12$$

where η is the complex white Gaussian noise whose standard deviation of both real and imaginary parts are 0.04. Using this noisy multi echo GRE signal I, the magnitude image and phase data are estimated

[1)] http://www.weill.cornell.edu/mri/pages/qsm.html
[2)] http://www.neuroimaging.at/pages/qsm.php

Table 3.1: Parameter selection for each dataset.

Dataset	Model	ν	λ	r	β
Brain phantom	1GHIRE (1.13)	2×10^{-4}	2.5×10^{-3}	·	0.05
	Model (1.14) $p = 1$	2×10^{-4}	1	·	0.05
	Model (1.14) $p = 2$	2×10^{-4}	10	·	0.05
	Model (2.6)	2×10^{-4}	·	160564	0.05
	2GHIRE (2.4)	2×10^{-4}	50	160564	0.05
SE data	1GHIRE (1.13)	2.5×10^{-5}	5×10^{-4}	·	0.05
	Model (1.14) $p = 1$	2.5×10^{-5}	0.125	·	0.05
	Model (1.14) $p = 2$	2.5×10^{-5}	1.25	·	0.05
	Model (2.6)	2.5×10^{-5}	·	81920	0.05
	2GHIRE (2.4)	2.5×10^{-5}	6.25	81920	0.05
ME data	1GHIRE (1.13)	2.5×10^{-5}	1.25×10^{-3}	·	0.05
	Model (1.14) $p = 1$	2.5×10^{-5}	0.125	·	0.05
	Model (1.14) $p = 2$	2.5×10^{-5}	1.25	·	0.05
	Model (2.6)	2.5×10^{-5}	·	393216	0.05
	2GHIRE (2.4)	2.5×10^{-5}	6.25	393216	0.05

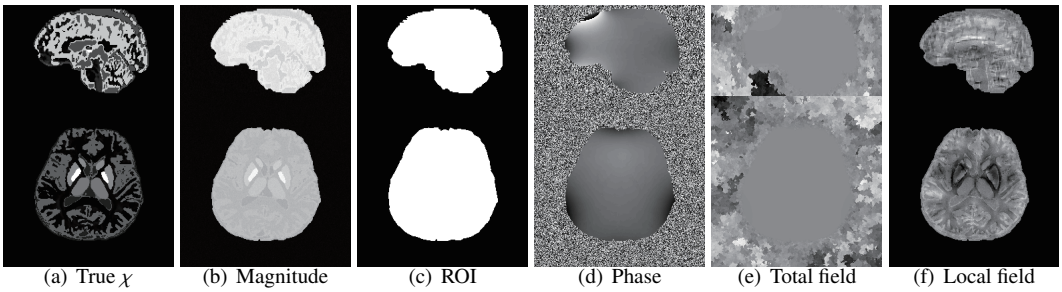

(a) True χ (b) Magnitude (c) ROI (d) Phase (e) Total field (f) Local field

Fig. 3.1. Images of synthesized datasets for the brain phantom experiments. The first row describes the sagittal slice images and the second row depicts the axial slice images.

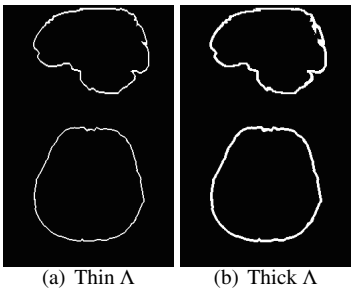

(a) Thin Λ (b) Thick Λ

Fig. 3.2. Images of estimated Λ for the brain phantom experiments. The first row describes the sagittal slice images and the second row depicts the axial slice images.

by the method in [50], and the phase is further unwrapped by the method in [51] to obtain the noisy and incomplete total field b. Then we solve the Poisson's equation (1.6) using the method in [52] to obtain the noisy local field data f (See Figure 3.1). Finally, for the comparison of the restored harmonic incompatibility v, we also solve (1.6) using $\widetilde{b}$ to obtain the true local field $\widetilde{f}$ and the true harmonic incompatibility $\widetilde{v}$ (See Figure 3.3).

Table 3.2 summarizes the RMSE and the SSIM of (1.13), (1.14), (2.6), and (2.4) for each choice of

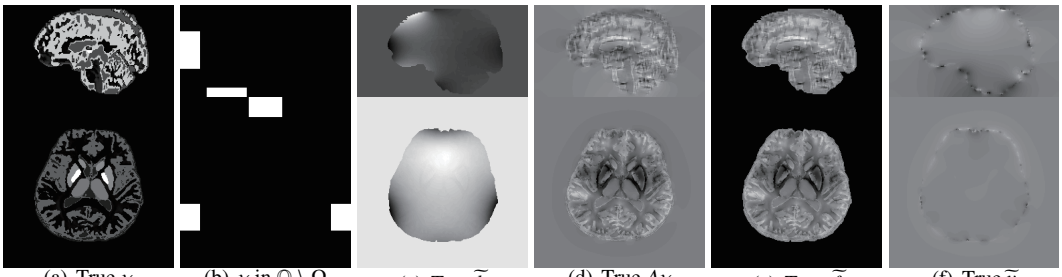

(a) True χ (b) χ in $\mathbb{O} \setminus \Omega$ (c) True $\widetilde{b}$ (d) True $A\chi$ (e) True $\widetilde{f}$ (f) True $\widetilde{v}$

Fig. 3.3. Reference noise-free datasets for the brain phantom experiments. The first row describes the sagittal slice images and the second row depicts the axial slice images.

Λ, and Figures 3.4 and 3.6 present visual comparisons of the results. We also visualize RMSE versus iteration number in Figure 3.9. We can see that, in any choice of Λ, the proposed 2GHIRE model (2.4) consistently outperforms the other reconstruction models. This demonstrates that we can further achieve better susceptibility reconstruction via better removal of the harmonic incompatibility, which arises from the background field removal stage to solve the Poisson's equation (1.6). Indeed, we can see that the 2GHIRE model (2.4) restores v better than other models with less singularities in Ω, as shown in Figures 3.5 and 3.7, leading to the improvements in both indices and visual quality. This means that by balancing the distance between $\mathcal{L}v$ which may not necessarily satisfy the constraint and w which satisfies the constraint, we can prevent v from capturing the outliers in Ω, achieving the better harmonic incompatibility removal. Indeed, since the ℓ_1 norm may not necessarily reflect the locally supported property of $\mathcal{L}v$, the 1GHIRE model in fact fails to remove the harmonic incompatibility in the local field data, as shown in Figure 3.5(b). In addition, we can see that the models (1.14) and (2.6) can also preserve where $\mathcal{L}v$ has to be nonzero. However, since the direct penalization can make $\mathcal{L}v$ capture the Laplacian of noise as well, they restore v inferior to the 2GHIRE model, as shown in Figures 3.5(c), 3.5(e), 3.7(c), and 3.7(e).

In order to further see the effect of Λ on the restoration results, we also present the zoom-in views of the axial slice images of Figures 3.4 and 3.6 in Figure 3.8. We can see that compared to the case of thin Λ, the models (1.14) and (2.6) results in the loss of information in Λ, as shown in Figures 3.8(c), 3.8(d), and 3.8(e), which agrees with the degradation of indices given in Table 3.2. In contrast, the 2GHIRE model yields visually identical results regardless of the choice of Λ, as shown in Figure 3.8(f), which again coincides the indices given in Table 3.2, thereby demonstrating the existence of basis mismatch arising from solving (1.6) and the robustness of the proposed 2GHIRE model to the estimation of the support of $\mathcal{L}v$.

Finally, we mention that compared to the other models, the 2GHIRE model requires approximately 50% of CPU times, as shown in Table 3.3. Most importantly, the iteration number of the 2GHIRE model is approximately 40% of the other reconstruction models. Even though the further theoretical convergence analysis will be needed, we can numerically observe that our proposed model reaches to a (local) minimum of the energy functional faster than other models. Therefore, we can conclude that the proposed 2GHIRE model (2.4) is able to achieve the better harmonic incompatibility removal robustly to the choice of Λ, together with the computational efficiency over the other models (1.13), (1.14), and (2.6).

Table 3.2: Comparison of relative error, and structural similarity index map for the brain phantom experiments

Λ	Indices	1GHIRE	(1.14) $p = 1$	(1.14) $p = 2$	(2.6)	2GHIRE
Thin	RMSE	0.4480	0.4403	0.4465	0.4403	**0.4281**
	SSIM	0.7436	0.7512	0.7494	0.7512	**0.7605**
Thick	RMSE	0.4480	0.4639	0.4699	0.4639	**0.4287**
	SSIM	0.7436	0.7450	0.7425	0.7450	**0.7600**

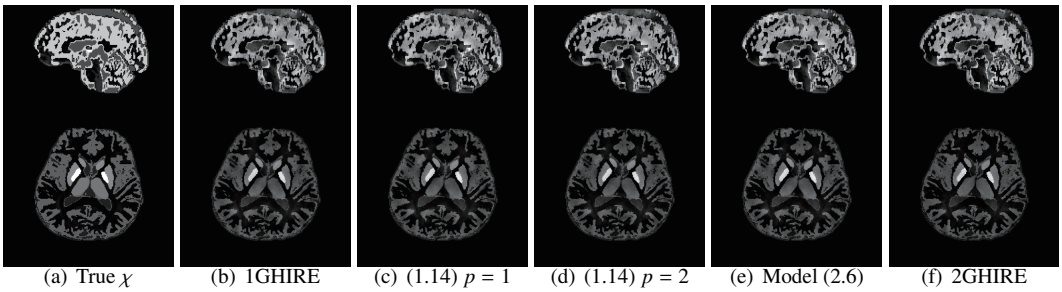

(a) True χ (b) 1GHIRE (c) (1.14) $p = 1$ (d) (1.14) $p = 2$ (e) Model (2.6) (f) 2GHIRE

Fig. 3.4. Images comparing QSM reconstruction methods for the brain phantom experiments with thin Λ. The first row describes the sagittal slice images, and the second row depicts the axial slice images. All sagittal slice images of brain phantom experimental results are displayed in the window level $[-0.03, 0.07]$, and the axial slice images of brain phantom experimental results are displayed in the window level $[-0.03, 0.19]$ for the fair comparison.

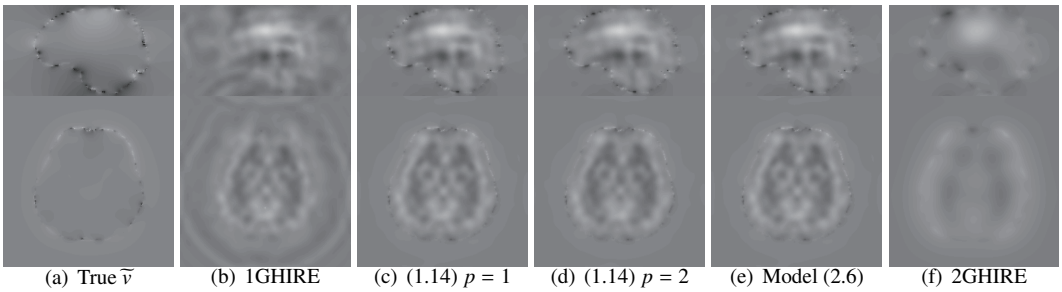

(a) True $\widetilde{v}$ (b) 1GHIRE (c) (1.14) $p = 1$ (d) (1.14) $p = 2$ (e) Model (2.6) (f) 2GHIRE

Fig. 3.5. Images of v for the brain phantom experiments with thin Λ. The first row describes the sagittal slice images and the second row depicts the axial slice images. The images of v for the brain phantom experiments are displayed in the window level $[-0.025, 0.025]$ for the fair comparison.

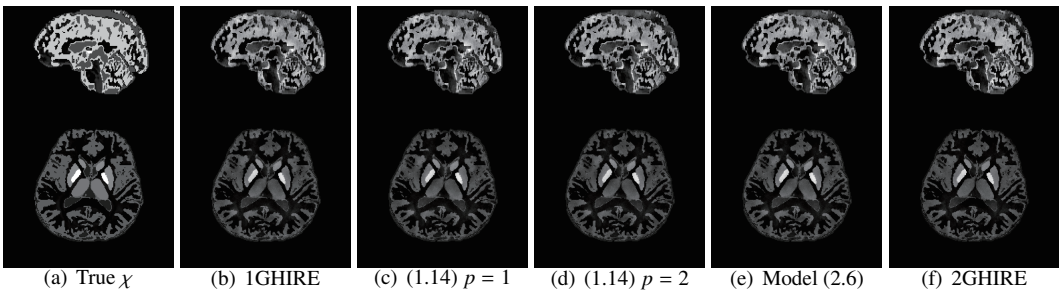

(a) True χ (b) 1GHIRE (c) (1.14) $p = 1$ (d) (1.14) $p = 2$ (e) Model (2.6) (f) 2GHIRE

Fig. 3.6. Images comparing QSM reconstruction methods for the brain phantom experiments with thick Λ. The first row describes the sagittal slice images and the second row depicts the axial slice images.

3.2. Single echo MR data experiments

The SE data experiments are conducted using $160\times160\times160$ image with spatial resolution $1.0625\times 1.0625\times 1.0714\text{mm}^3$, which is obtained from a 3T MR system and which can be downloaded on Neu-

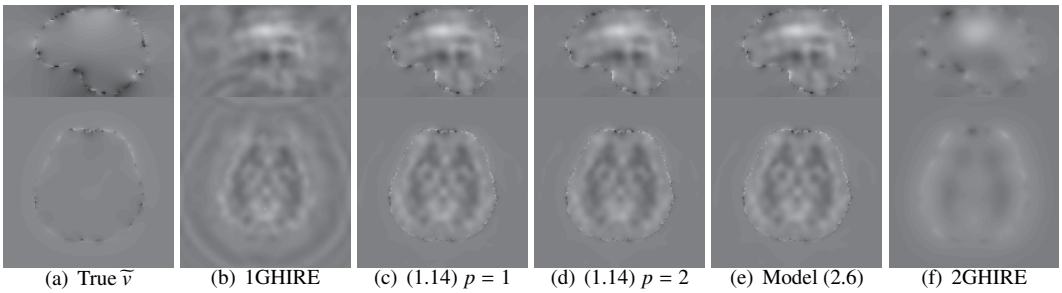

(a) True $\widetilde{v}$ (b) 1GHIRE (c) (1.14) $p = 1$ (d) (1.14) $p = 2$ (e) Model (2.6) (f) 2GHIRE

Fig. 3.7. Images of v for the brain phantom experiments with thick Λ. The first row describes the sagittal slice images and the second row depicts the axial slice images.

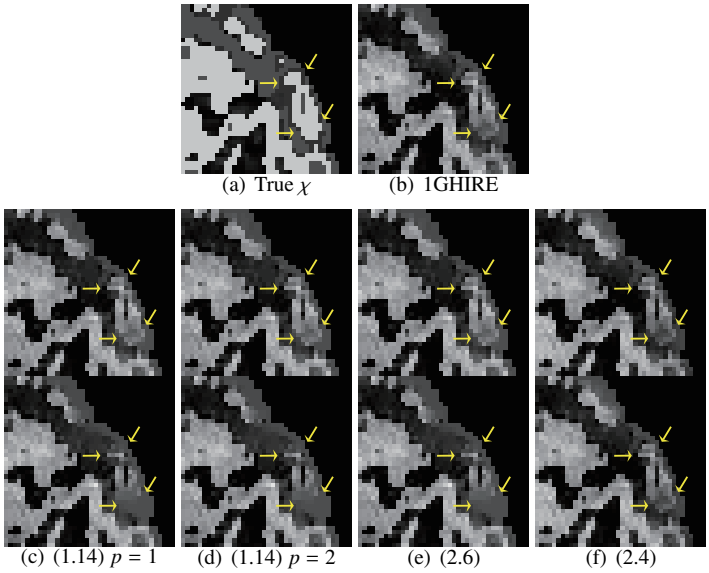

(a) True χ (b) 1GHIRE

(c) (1.14) $p = 1$ (d) (1.14) $p = 2$ (e) (2.6) (f) (2.4)

Fig. 3.8. Comparison of Figures 3.4 and 3.6. The first row uses thin Λ, and the second row uses the thick Λ. The yellow arrows indicate the regions worth noticing.

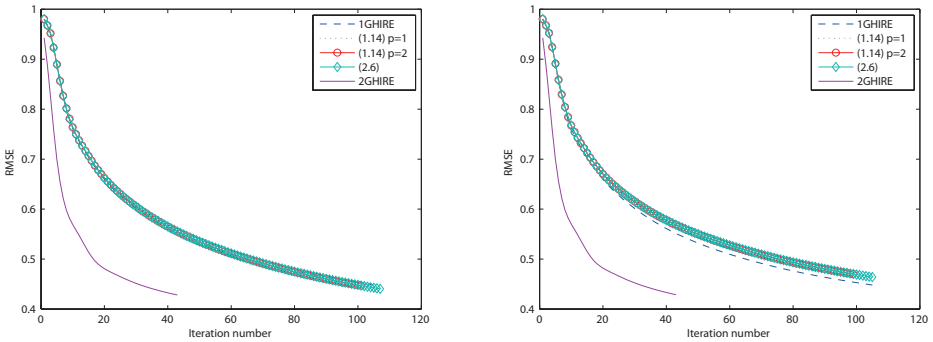

(a) Thin Λ (b) Thick Λ

Fig. 3.9. RMSE versus iteration number for the brain phantom experiments.

roimaging Research Unit-Medical University of Graz webpage. We unwrap the phase in Figure 3.10(d) using the Laplacian based phase unwrapping in [48] to obtain the total field data in Figure 3.10(e). Then

Table 3.3: Comparison of the number of iterations and the CPU time for the brain phantom experiments

Λ	Indices	1GHIRE	(1.14) $p = 1$	(1.14) $p = 2$	(2.6)	2GHIRE
Thin	# of Iter	105	107	101	107	43
	CPU Time	400.83	409.22	386.08	471.47	191.36
Thick	# of Iter	105	105	99	107	43
	CPU Time	400.83	405.33	380.49	465.99	192.56

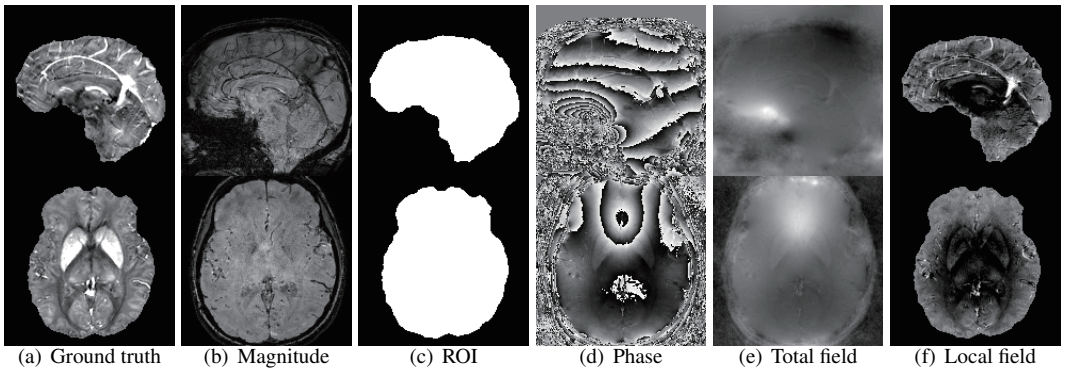

(a) Ground truth (b) Magnitude (c) ROI (d) Phase (e) Total field (f) Local field

Fig. 3.10. Images of single echo datasets. The first row describes the sagittal slice images and the second row depicts the axial slice images.

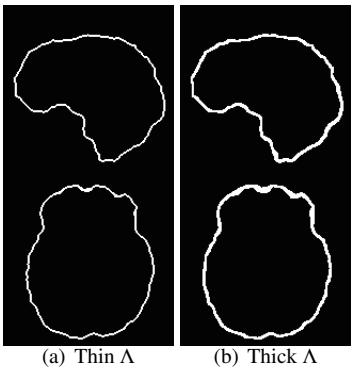

(a) Thin Λ (b) Thick Λ

Fig. 3.11. Images of estimated Λ for the SE data experiments. The first row describes the sagittal slice images and the second row depicts the axial slice images.

we solve the Poisson's equation (1.6) by the method in [52] to further obtain the measured local field data f in Figure 3.10(f). Here, the ground truth image in Figure 3.10(a) is obtained by the calculation of susceptibility using multiple orientation sampling (COSMOS) method in [15] using the 12 orientation data.

Table 3.4 summarizes the RMSE and the SSIM of (1.13),(1.14) with both $p = 1$ and $p = 2$, (2.6) and (2.4) for each choice of Λ, Figures 3.12 and 3.14 present visual comparisons of the results, and RMSE versus iteration number is given in Figure 3.16. The number of iterations and the CPU times are given in Table 3.5 as well. We can see that the overall results are almost similar to the brain phantom experiments, including the robustness to the choice of Λ as well as the computational efficiency. It is also worth noting that the 2GHIRE model can reduce the shadow artifacts in all directions, as shown in Figures 3.12(f) and 3.14(f). Indeed, as we can see from Figure 3.12(b), even though the previous 1GHIRE removes the shadow artifacts along the sagittal slice direction, the axial slice images have a degradation in the contrasts as shown in Figure 3.12(b). In addition, even though the models (1.14)

Table 3.4: Comparison of relative error, and structural similarity index map for the SE data experiments

Λ	Indices	1GHIRE	(1.14) $p = 1$	(1.14) $p = 2$	(2.6)	2GHIRE
Thin	RMSE	0.8025	0.8141	0.7538	0.8141	**0.6995**
	SSIM	0.8085	**0.8298**	0.8248	**0.8298**	0.8289
Thick	RMSE	0.8025	0.8077	0.7530	0.8074	**0.7004**
	SSIM	0.8085	0.8213	0.8236	0.8213	**0.8288**

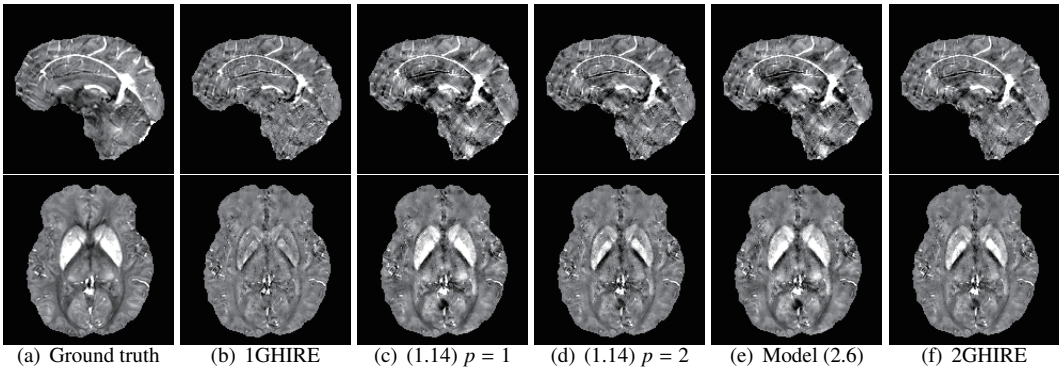

(a) Ground truth (b) 1GHIRE (c) (1.14) $p = 1$ (d) (1.14) $p = 2$ (e) Model (2.6) (f) 2GHIRE

Fig. 3.12. Images comparing QSM reconstruction methods for the SE data experiments with thin Λ. The first row describes the sagittal slice images and the second row depicts the axial slice images. All reconstructed images of SE data experiments are displayed in the window level $[-0.1, 0.1]$.

Table 3.5: Comparison of the number of iterations and the CPU time for the SE data experiments

Λ	Indices	1GHIRE	(1.14) $p = 1$	(1.14) $p = 2$	(2.6)	2GHIRE
Thin	# of Iter	80	152	86	152	59
	CPU Time	238.07	449.73	253.66	506.03	200.76
Thick	# of Iter	80	152	87	152	59
	CPU Time	238.07	448.38	252.84	500.69	200.03

and (2.6) restore the sagittal slice images with better contrast, the sagittal slice images contain shadow artifacts as shown in Figures 3.12(c), 3.14(c), 3.12(d), 3.14(d), 3.12(e) , and 3.14(e). In contrast, the 2GHIRE model (2.4) can achieve the better artifact removal together with less degradation in contrasts, leading to the performance gain.

We also compare the harmonic incompatibilities restored by each model in Figures 3.13 and 3.15. Compared to the 1GHIRE (1.13), it seems that the 2GHIRE (2.4) as well as (1.14) and (2.6) better restore v in the interior of Ω. However, we can also see that the models (1.14) and (2.6) restore v which is discontinuous across the interface between Ω and $\mathbb{O} \setminus \Omega$, as shown in Figures 3.13(b), 3.15(b), 3.13(c), 3.15(c), 3.13(d), and 3.15(d), while the 2GHIRE model restores v which is continuous along the interface (Figures 3.13(e) and 3.15(e)). As already mentioned in subsection 1.1, the harmonic incompatibility v (in the continuous domain) satisfies (1.10), (1.11), and (1.12). Hence, it has to be continuous on $\partial\Omega$. In addition, since the discrete HIRE models are based on the characterizations of v in continuous domain, the restoration results are desired to be mostly coincident with the theoretical discoveries as well. However, since both (1.14) and (2.6) fail to reconstruct v which agrees with our theoretical discovery, such an erroneous restoration of v in turn leads to another shadow artifacts in the reconstructed susceptibility image. Hence, in the SE data experiments, we can arrive at the similar conclusion to the brain phantom experiments.

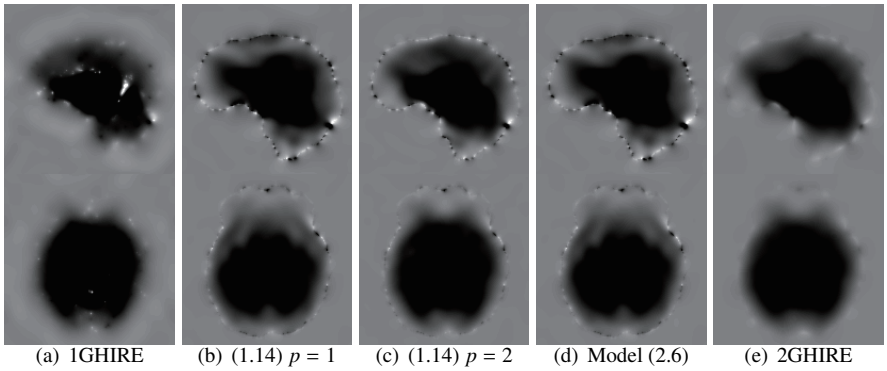

(a) 1GHIRE (b) (1.14) $p = 1$ (c) (1.14) $p = 2$ (d) Model (2.6) (e) 2GHIRE

Fig. 3.13. Images of v for the single echo MR data experiments with thin Λ. The first row describes the sagittal slice images and the second row depicts the axial slice images. The images of v for the SE data experiments are displayed in the window level $[-0.025, 0.025]$ for the fair comparison.

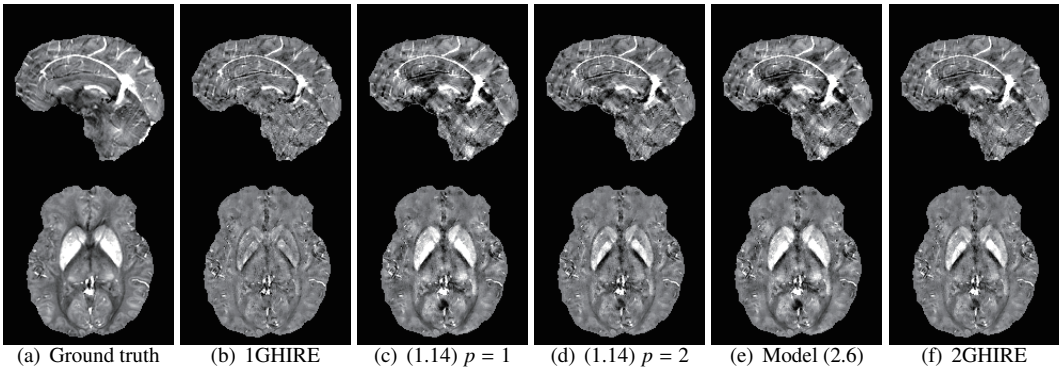

(a) Ground truth (b) 1GHIRE (c) (1.14) $p = 1$ (d) (1.14) $p = 2$ (e) Model (2.6) (f) 2GHIRE

Fig. 3.14. Images comparing QSM reconstruction methods for the single echo MR data experiments with thick Λ. The first row describes the sagittal slice images and the second row depicts the axial slice images.

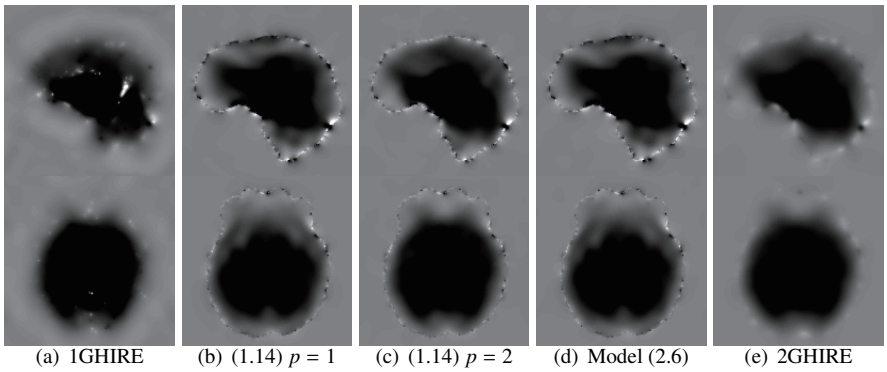

(a) 1GHIRE (b) (1.14) $p = 1$ (c) (1.14) $p = 2$ (d) Model (2.6) (e) 2GHIRE

Fig. 3.15. Images of v for the single echo MR data experiments with thick Λ. The first row describes the sagittal slice images and the second row depicts the axial slice images.

3.3. Multi echo MR data experiments

The ME data experiments are conducted using $512 \times 512 \times 200$ image with spatial resolution $0.46875 \times 0.46875 \times 0.7\text{mm}^3$, which is obtained from a 3T MR system. More precisely, 12 equispaced multi echo GRE sequences with TE ranging from 3.8msec to 48.9msec and time of relaxation

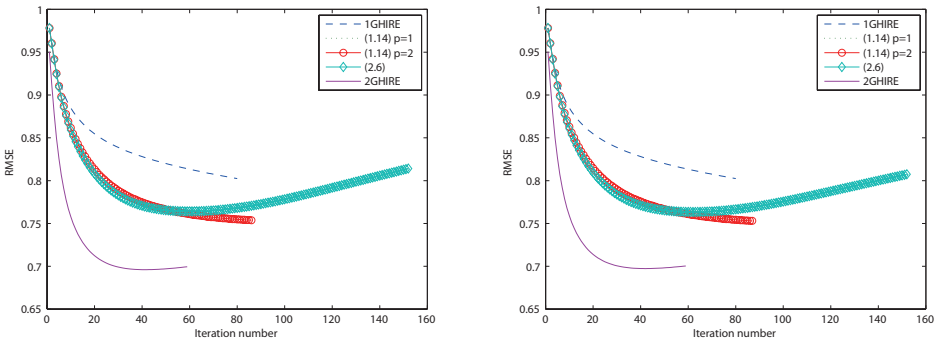

(a) Thin Λ (b) Thick Λ

Fig. 3.16. RMSE versus iteration number for the single echo MR data experiments.

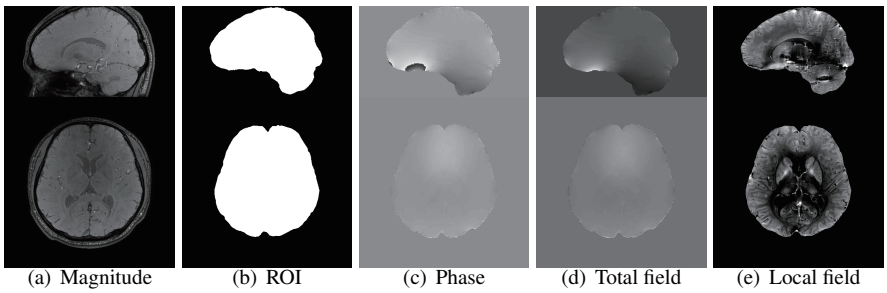

(a) Magnitude (b) ROI (c) Phase (d) Total field (e) Local field

Fig. 3.17. Images of ME datasets. The first row describes the sagittal slice images and the second row depicts the axial slice images.

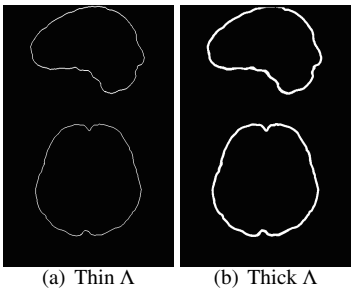

(a) Thin Λ (b) Thick Λ

Fig. 3.18. Images of estimated Λ for the ME data experiments. The first row describes the sagittal slice images and the second row depicts the axial slice images.

53.2msec. We first unwrap the phase data in Figure 3.17(c) to obtain total field data in Figure 3.17(d), and then we solve the Poisson's equation (1.6) using the method in [52] to obtain the local field data f in Figure 3.17(e).

Figures 3.19 and 3.21 display the visual comparisons of (1.13),(1.14) with both $p = 1$ and $p = 2$, (2.6) and (2.4) for each choice of Λ. Since the reference image is not available for in the ME data, it is in general more difficult to provide quantitative evaluations than the previous two cases. Nonetheless, we can see from the viewpoint of visual comparison that the pros and cons are almost the same as the numerical brain phantom experiments and the SE data experiments. We also compare the harmonic incompatibilities reconstructed by each model with different choice of Λ in Figures 3.20 and 3.22. It is worth noting that compared to other reconstruction models, the 2GHIRE model reconstructs v less containing the outliers in Λ. As previously mentioned in [21, Theorem 2.2], the harmonic incompati-

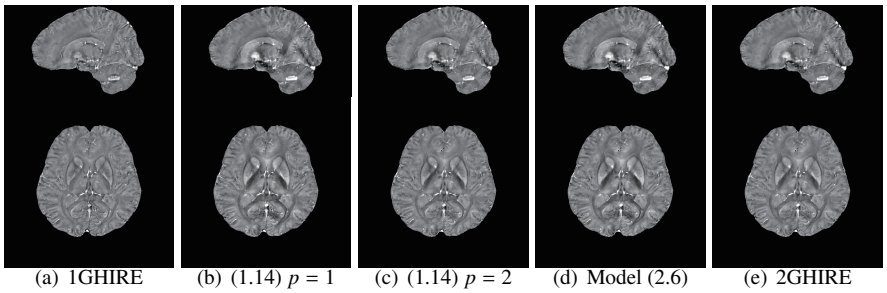

(a) 1GHIRE (b) (1.14) $p = 1$ (c) (1.14) $p = 2$ (d) Model (2.6) (e) 2GHIRE

Fig. 3.19. Images comparing QSM reconstruction methods for the ME data experiments with thin Λ. The first row describes the sagittal slice images and the second row depicts the axial slice images. All reconstructed images for ME data experiments are displayed in the window level $[-0.5, 0.5]$.

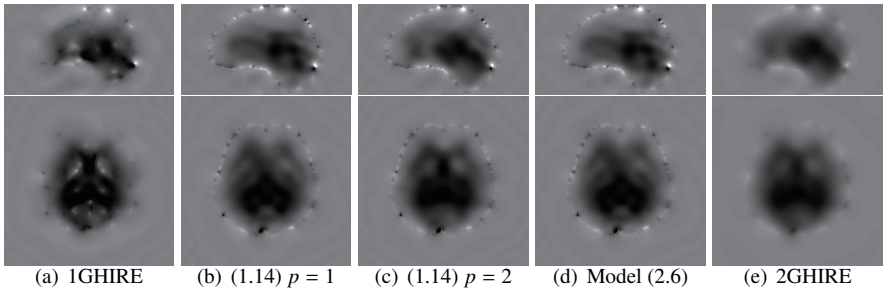

(a) 1GHIRE (b) (1.14) $p = 1$ (c) (1.14) $p = 2$ (d) Model (2.6) (e) 2GHIRE

Fig. 3.20. Images of v for the ME data experiments with thin Λ. The first row describes the sagittal slice images and the second row depicts the axial slice images. The images of v for the ME data experiments are displayed in the window level $[-0.15, 0.15]$ for the fair comparison.

bility v is induced by the Dirichlet boundary condition of (1.6), i.e. by information of (unknown) $-A\chi$ on $\partial\Omega$. However, since the models (1.14) and (2.6) restore a harmonic function induced by the outliers, such an erroneous reconstruction of v eventually generates another incompatibility in the low frequency components of f, leading to the shadow artifacts in the reconstructed image. In contrast, since the term $\|\mathcal{L}v - w\|_2^2$ keeps the distance between $\mathcal{L}v$ and w (containing the Laplacian of outliers), the 2GHIRE model is likely to make v on the boundary closer to $A\chi$, leading to the better harmonic incompatibility removal.

We further mention that compared to the noticeable differences in v among the reconstruction models, the differences in the reconstructed susceptibility images are relatively marginal. One possible reason would be the outliers in the measured local field data lying in the ROI Ω. As mentioned in [12], the local field data is prone to outliers where the MRI image has a low SNR. Moreover, in the region where the MRI image contains outliers, the phase unwrapping stage may introduce outliers in the total field data in the same region [19]. In any case, the forward model (2.1) does not hold in that region any more, so the susceptibility reconstruction model will need improving so that such outliers can be suppressed at the same time. Moreover, it is known in the literature that the susceptibility of the white matter is anisotropic, i.e. χ is a 3×3 symmetric tensor in the white matter [44]. Since (2.1) does not hold in this case either, we may need to remove the effect of anisotropic susceptibility for the better susceptibility reconstruction as a future work. Finally, compared to the smallest number of iterations, the CPU time for the 2GHIRE model is relatively long. This indicates that the implementation of Algorithm 2.1 has to be further improved so that the application to the high resolution MR data is also available with high computational efficiency.

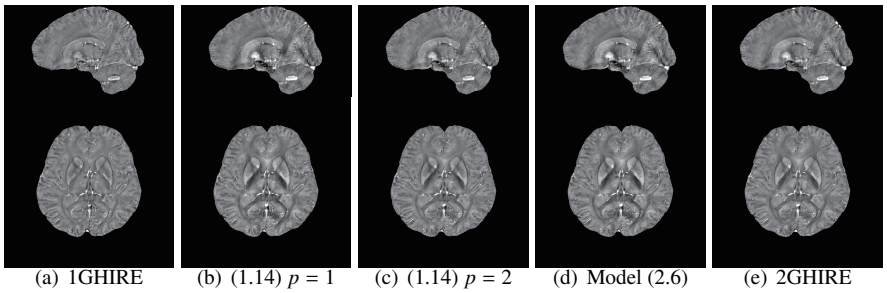

(a) 1GHIRE (b) (1.14) $p = 1$ (c) (1.14) $p = 2$ (d) Model (2.6) (e) 2GHIRE

Fig. 3.21. Images comparing QSM reconstruction methods for the ME data experiments with thick Λ. The first row describes the sagittal slice images and the second row depicts the axial slice images.

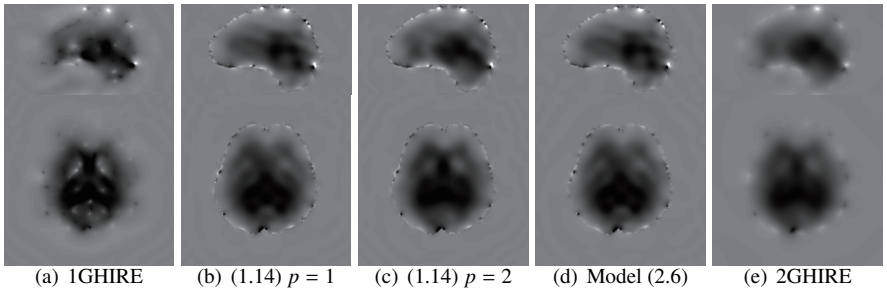

(a) 1GHIRE (b) (1.14) $p = 1$ (c) (1.14) $p = 2$ (d) Model (2.6) (e) 2GHIRE

Fig. 3.22. Images of v for the ME data experiments with thick Λ. The first row describes the sagittal slice images and the second row depicts the axial slice images.

Table 3.6: Comparison of the number of iterations and the CPU time for the ME data experiments.

Λ	Indices	1GHIRE	(1.14) $p = 1$	(1.14) $p = 2$	(2.6)	2GHIRE
Thin	# of Iter	90	107	85	107	75
	CPU Time	3038.80	3619.58	3105.35	4635.73	3286.33
Thick	# of Iter	90	105	85	105	75
	CPU Time	3038.80	4042.78	3173.09	4440.30	3204.26

4. Conclusion and future directions

In this paper, we proposed a new harmonic incompatibility removal model for the susceptibility imaging. The proposed 2GHIRE model is inspired by the balanced approach in the wavelet frame image restoration which provides a flexibility in the sparse representation and the regularity of an image. More precisely, since the discrete grid and the discrete data are available only, the basis mismatch arising from solving (1.6) numerically is inevitable. However, by promoting a flexibility between the $\mathcal{L}v$ and w which satisfies (2.2) and (2.3), we can achieve the better artifact suppression in the reconstructed susceptibility image as well as the robustness to the estimation of $\mathrm{supp}(\mathcal{L}v)$. Finally, the experimental results show that the proposed approach (2.4) outperforms the previous 1GHIRE model (1.13) in [21] as well as its variants in both brain phantom and in vivo MR data.

For the future work, we will consider taking the anisotropic susceptibility (i.e. 3×3 symmetric susceptibility tensor) in the white matter into account for the better coincidence with the real cases. Since such an anisotropic susceptibility already destroys the forward model of QSM, it is necessary to consider the anisotropy correction to overcome the bottleneck in restoration performance. It would be also interesting to apply the idea of harmonic incompatibility removal into the susceptibility tensor imaging [44], which aims to reconstruct a 3×3 symmetric susceptibility tensor image.

Acknowledgments

The authors would like to thank the authors in [12, 18, 44, 45] for providing the in vivo MR datasets and the MATLAB toolbox so that the experiments can be implemented. The authors also thank the anonymous reviewers for their constructive suggestions and comments that helped tremendously with improving the presentation of this paper.

References

[1] L.de Rochefort, T. Liu, B. Kressler, J. Liu, P. Spincemaille, V. Lebon, J. Wu and Y. Wang, Quantitative susceptibility map reconstruction from MR phase data using Bayesian regularization: validation and application to brain imaging, *Magn. Reson. Med.*, **63**:1 (2010), 194–206.

[2] J.K. Seo, E.J. Woo, U. Katscher and Y. Wang, Electro-Magnetic Tissue Properties MRI, Imperial College Press, London, 1st edition, 2014.

[3] Y. Kee, Z. Liu, L. Zhou, A. Dimov, J. Cho, L.de Rochefort, J.K. Seo and Y. Wang, Quantitative susceptibility mapping (QSM) algorithms: mathematical rationale and computational implementations, *IEEE Trans. Biomed. Eng.*, **64**:11 (2017), 2531–2545.

[4] W. Chen, S.A. Gauthier, A. Gupta, J. Comunale, T. Liu, S. Wang, M. Pei, D. Pitt and Y. Wang, Quantitative susceptibility mapping of multiple sclerosis lesions at various ages, *Radiology*, **271**:1 (2014), 183–192, PMID: 24475808.

[5] J. Acosta-Cabronero, G.B. Williams, A. Cardenas-Blanco, R.J. Arnold, V. Lupson and P.J. Nestor, In vivo quantitative susceptibility mapping (QSM) in Alzheimer's disease, *PloS one*, **8**:11 (2013), e81093.

[6] J.M.G.van Bergen, J. Hua, P.G. Unschuld, I.A.L. Lim, C.K. Jones, R.L. Margolis, C.A. Ross, P.C.M.van Zijl and X. Li, Quantitative susceptibility mapping suggests altered brain iron in premanifest Huntington disease, *Amer. J. Neuroradiol*, **37**:5 (2016), 789–796.

[7] E.M. Haacke, J. Tang, J. Neelavalli and Y.C.N. Cheng, Susceptibility mapping as a means to visualize veins and quantify oxygen saturation, *J. Magn. Reson. Imag.*, **32**:3 (2010), 663–676.

[8] J. Klohs, A. Deistung, F. Schweser, J. Grandjean, M. Dominietto, C. Waschkies, R.M. Nitsch, I. Knuesel, J.R. Reichenbach and M. Rudin, Detection of cerebral microbleeds with quantitative susceptibility mapping in the arcabeta mouse model of cerebral amyloidosis, *J. Cerebr. Blood F. Met.*, **31**:12 (2011), 2282–2292, PMID: 21847134.

[9] A.V. Dimov, Z. Liu, P. Spincemaille, M.R. Prince, J. Du and Y. Wang, Bone quantitative susceptibility mapping using a chemical species? Specific r2* signal model with ultrashort and conventional echo data, *Magn. Reson. Med.*, **79**:1 (2018), 121–128.

[10] T. Liu, P. Spincemaille, L.de Rochefort, R. Wong, M. Prince and Y. Wang, Unambiguous identification of superparamagnetic iron oxide particles through quantitative susceptibility mapping of the nonlinear response to magnetic fields, *Magn. Reson. Imaging*, **28**:9 (2010), 1383 – 1389.

[11] C. Milovic, B. Bilgic, B. Zhao, C. Langkammer, C. Tejos and J. Acosta-Cabronero, Weak-harmonic regularization for quantitative susceptibility mapping, *Magn. Reson. Med.*, **81**:2 (2019), 1399–1411.

[12] Y. Wang and T. Liu, Quantitative susceptibility mapping (QSM): decoding MRI data for a tissue magnetic biomarker, *Magn. Reson. Med.*, **73**:1 (2015), 82–101.

[13] T. Liu, I. Khalidov, L.de Rochefort, P. Spincemaille, J. Liu, A.J. Tsiouris and Y. Wang, A novel background field removal method for MRI using projection onto dipole fields (PDF), *NMR Biomed*, **24**:9 (2011), 1129–1136.

[14] T. Liu, J. Liu, L.de Rochefort, P. Spincemaille, I. Khalidov, J.R. Ledoux and Y. Wang, Morphology enabled dipole inversion (MEDI) from a single-angle acquisition: comparison with COSMOS in human brain imaging, *Magn. Reson. Med.*, **66**:3 (2011), 777–783.

[15] T. Liu, P. Spincemaille, L.de Rochefort, B. Kressler and Y. Wang, Calculation of susceptibility through multiple orientation sampling (COSMOS): a method for conditioning the inverse problem from measured magnetic field map to susceptibility source image in MRI, *Magn. Reson. Med.*, **61**:1 (2009), 196–204.

[16] E.M. Stein and R. Shakarchi, Functional Analysis. Introduction to Further Topics in Analysis, volume 4 of *Princeton Lect. Anal.*, Princeton University Press, Princeton, NJ, 2011.

[17] E.M. Haacke, S. Liu, S. Buch, W. Zheng, D. Wu and Y. Ye, Quantitative susceptibility mapping: current status and future directions, *Magn. Reson. Imaging*, **33**:1 (2015), 1 – 25.

[18] J.K. Choi, H.S. Park, S. Wang, Y. Wang and J.K. Seo, Inverse problem in quantitative susceptibility mapping, *SIAM J. Imaging Sci.*, **7**:3 (2014), 1669–1689.

[19] T. Liu, C. Wisnieff, M. Lou, W. Chen, P. Spincemaille and Y. Wang, Nonlinear formulation of the magnetic field to source relationship for robust quantitative susceptibility mapping, *Magn. Reson. Med.*, **69**:2 (2013), 467–476.

[20] S. Wang, T. Liu, W. Chen, P. Spincemaille, C. Wisnieff, A.J. Tsiouris, W. Zhu, C. Pan, L. Zhao and Y. Wang, Noise effects in various quantitative susceptibility mapping methods, *IEEE Trans. Biomed. Eng.*, **60**:12 (2013), 3441–3448.

[21] C. Bao, J. Choi and B. Dong, Whole brain susceptibility mapping using harmonic incompatibility removal, *SIAM J. Imaging Sci.*, **12**:1 (2019), 492–520.

[22] F. Trèves, Basic Linear Partial Differential Equations, Dover Publications, Inc., Mineola, NY, 2006, Reprint of the 1975 original.

[23] H. Sun and A.H. Wilman, Background field removal using spherical mean value filtering and tikhonov regularization, *Magn. Reson. Med.*, **71**:3 (2014), 1151–1157.

[24] L.C. Evans, Partial Differential Equations, volume 19 of *Graduate Studies in Mathematics*, American Mathematical Society, Providence, RI, second edition, 2010.

[25] H. Ji and K. Wang, Robust image deblurring with an inaccurate blur kernel, *IEEE Trans. Image Process.*, **21**:4 (2012), 1624–1634.

[26] J. Li, C. Miao, Z. Shen, G. Wang and H. Yu, Robust frame based x-ray CT reconstruction, *J. Comput. Math.*, **34**:6 (2016), 683–704.

[27] J.F. Cai, R.H. Chan, L. Shen and Z. Shen, Convergence analysis of tight framelet approach for missing data recovery, *Adv. Comput. Math.*, **31**:1-3 (2009), 87–113.

[28] J.F. Cai, R.H. Chan and Z. Shen, Simultaneous cartoon and texture inpainting, *Inverse Probl. Imaging*, **4**:3 (2010), 379–395.

[29] R.H. Chan, T.F. Chan, L. Shen and Z. Shen, Wavelet algorithms for high-resolution image reconstruction, *SIAM J. Sci. Comput.*, **24**:4 (2003), 1408–1432.

[30] J.F. Cai, T. Wang and K. Wei, Fast and provable algorithms for spectrally sparse signal reconstruction via low-rank Hankel matrix completion, *Appl. Comput. Harmon. Anal.*, **46**:1 (2019), 94–121.

[31] G. Ongie and M. Jacob, Off-the-grid recovery of piecewise constant images from few Fourier samples, *SIAM J. Imaging Sci.*, **9**:3 (2016), 1004–1041.

[32] C. Milovic, B. Bilgic, B. Zhao, J. Acosta-Cabronero and C. Tejos, Fast nonlinear susceptibility inversion with variational regularization, *Magn. Reson. Med.*, **80**:2 (2018), 814–821.

[33] J.F. Cai, B. Dong, S. Osher and Z. Shen, Image restoration: total variation, wavelet frames, and beyond, *J. Amer. Math. Soc.*, **25**:4 (2012), 1033–1089.

[34] J.F. Cai, B. Dong and Z. Shen, Image restoration: a wavelet frame based model for piecewise smooth functions and beyond, *Appl. Comput. Harmon. Anal.*, **41**:1 (2016), 94–138.

[35] L.I. Rudin, S. Osher and E. Fatemi, Nonlinear total variation based noise removal algorithms, *Phys. D*, **60**:1-4 (1992), 259–268, Experimental mathematics: computational issues in nonlinear science (Los Alamos, NM, 1991).

[36] K. Bredies, K. Kunisch and T. Pock, Total generalized variation, *SIAM J. Imaging Sci.*, **3**:3 (2010), 492–526.

[37] Y. Kee, J. Cho, K. Deh, Z. Liu, P. Spincemaille and Y. Wang, Coherence enhancement in quantitative susceptibility mapping by means of anisotropic weighting in morphology enabled dipole inversion, *Magn. Reson. Med.*, **79**:2 (2018), 1172–1180.

[38] Z. Liu, P. Spincemaille, Y. Yao, Y. Zhang and Y. Wang, MEDI+0: morphology enabled dipole inversion with automatic uniform cerebrospinal fluid zero reference for quantitative susceptibility mapping, *Magn. Reson. Med.*, **79**:5 (2017), 2795–2803.

[39] J. Eckstein and D.P. Bertsekas, On the Douglas-Rachford splitting method and the proximal point algorithm for maximal monotone operators, *Math. Programming*, **55**:3, Ser. A (1992), 293–318.

[40] J.F. Cai, S. Osher and Z. Shen, Split Bregman methods and frame based image restoration, *Multiscale Model. Simul.*, **8**:2 (2009/10), 337–369.

[41] T. Goldstein and S.J. Osher, The split Bregman method for $L1$-regularized problems, *SIAM J. Imaging Sci.*, **2**:2 (2009), 323–343.

[42] Y.R. Fan, T.Z. Huang, T.H. Ma and X.L. Zhao, Cartoon-texture image decomposition via non-convex low-rank texture regularization, *J. Franklin Inst.*, **354**:7 (2017), 3170–3187.

[43] B. He, M. Tao and X. Yuan, Alternating direction method with Gaussian back substitution for separable convex programming, *SIAM J. Optim.*, **22**:2 (2012), 313–340.

[44] C. Wisnieff, T. Liu, P. Spincemaille, S. Wang, D. Zhou and Y. Wang, Magnetic susceptibility anisotropy: cylindrical symmetry from macroscopically ordered anisotropic molecules and accuracy of MRI measurements using few orientations, *NeuroImage*, **70** (2013), 363 – 376.

[45] C. Langkammer, F. Schweser, K. Shmueli, C. Kames, X. Li, L. Guo, C. Milovic, J. Kim, H. Wei, K. Bredies, S. Buch, Y. Guo, Z. Liu, J. Meineke, A. Rauscher, J.P. Marques and B. Bilgic, Quantitative susceptibility mapping: Report from the 2016 reconstruction challenge, *Magn. Reson. Med.*, **79**:3 (2018), 1661–1673.

[46] K. Shmueli, J.A.de Zwart, P.van Gelderen, T. Li, S.J. Dodd and J.H. Duyn, Magnetic susceptibility mapping of brain tissue in vivo using MRI phase data, *Magn. Reson. Med.*, **62**:6 (2009), 1510–1522.

[47] B. Kressler, L.de Rochefort, T. Liu, P. Spincemaille, J. Quan and Y. Wang, Nonlinear regularization for per voxel estimation of magnetic susceptibility distributions from MRI field maps, *IEEE Trans. Med. Imag.*, **29**:2 (2010), 273–281.

[48] W. Li, A.V. Avram, B. Wu, X. Xiao and C. Liu, Integrated Laplacian-based phase unwrapping and background phase removal for quantitative susceptibility mapping, *NMR in Biomedicine*, **27**:2 (2014), 219–227, NBM-13-0182.R2.

[49] Z. Wang, A.C. Bovik, H.R. Sheikh and E.P. Simoncelli, Image quality assessment: from error visibility to structural similarity, *IEEE Trans. Image Process.*, **13**:4 (2004), 600–612.

[50] L.de Rochefort, R. Brown, M.R. Prince and Y. Wang, Quantitative MR susceptibility mapping using piece-wise constant regularized inversion of the magnetic field, *Magn. Reson. Med.*, **60**:4 (2008), 1003–1009.

[51] D.C. Ghiglia and M.D. Pritt, Two-Dimensional Phase Unwrapping: Theory, Algorithms, and Software, Wiley-Interscience publication, Wiley, 1998.

[52] D. Zhou, T. Liu, P. Spincemaille and Y. Wang, Background field removal by solving the Laplacian boundary value problem, *NMR in Biomedicine*, **27**:3 (2014), 312–319, NBM-13-0115.R3.